NUCET NUCLEAR ENERGY AND TECHNOLOGY

Nuclear Energy and Technology 11(1): 43–53
DOI 10.3897/nucet.11.139558

Research Article

Tungsten wires with steel matrix composite: wetting and infiltration by steel melt

Nikita Popov[1], Alexey Suchkov[1], Mikhail Zharkov[1,2], Veronika Kirillova[1], Alexander Bazhenov[1], Pavel Dzhumaev[1], Alexey Vertkov[2], Oleg Sevryukov[1]

1 *National Research Nuclear University MEPhI (Moscow Engineering Physics Institute), Kashirskoye Shosse, 31, 115409 Moscow, Russia*
2 *Joint-Stock Company "N.A. Dollezhall Research and Development Institute of Power Engineering", (JSC "NIKIET"), Malaya Krasnoselskaya 2/8, 107140, Moscow, Russia*

Corresponding author: Nikita Popov (NSPopov@mephi.ru)

Academic editor: Yury Korovin ◆ **Received** 17 October 2024 ◆ **Accepted** 13 January 2025 ◆ **Published** 14 February 2025

Citation: Popov N, Suchkov A, Zharkov M, Kirillova V, Bazhenov A, Dzhumaev P, Vertkov A, Sevryukov O (2025) Tungsten wires with steel matrix composite: wetting and infiltration by steel melt. Nuclear Energy and Technology 11(1): 43–53. https://doi.org/10.3897/nucet.11.139558

Abstract

Lithium-based capillary porous systems (CPS) made of tungsten mesh are a part of the most prospective approach to plasma facing components. Currently, tungsten mesh as a part of the CPS is mounted directly on the experimental assembly without a proper joining with a substrate. Tungsten mesh filled with steel could be used as a base structure for the CPS. The experiment considers the wetting of tungsten by steel melt and the features of short- and long-term interaction between the two materials. Wetting was studied by improved sessile drop experiment. The results show that an average contact angle is 69° for SS316LN and 83.2° for SS420 melt on tungsten substrate with a temperature of 500–650 °C. Tungsten-steel composite was manufactured by infiltration of tungsten mesh with a steel melt. As a result of an active dissolution of tungsten in steel melt, $(Fe,Cr)_7W_6$ interaction layer with a thickness up to 10 µm forms around tungsten. Optimal structure with the thinnest intermetallic layer is obtained in the zones with the lowest temperature and the highest cooling speed.

Keywords

steel, tungsten, composite, wetting, armor block

Introduction

Tungsten is a common plasma facing material (PFM) for the divertor armor block in experimental thermonuclear facilities. High thermal conductivity, high melting point, low sputtering, low tritium retention and the ability to withstand heat fluxes up to 20 MW/m^2 are the most important properties of a tungsten-based plasma facing material (PFC) (Gago et al. 2020; Du n.d.). ITER Organization plans to shift the first wall material from beryllium to tungsten in order to reduce the tritium's retention inside the ITER vessel and dust production while also increasing the resilience of in-vessel components against disruptions. Considering high sputtering rate of Be (Guseva et al. 1999), this improves the operation safety. The main disadvantage of tungsten and its alloys is the processability and cost of production.

Tungsten demonstrates high performance as a PFM, however there some are fundamental difficulties regarding the solid PFC concept. Any solid material sputters and contaminates the plasma due to the inevitable contact with plasma during the sudden disruptions and instabilities. A

PFC based on a liquid metal approach is able to negate the sputtering and contamination of plasma with the atoms of the first wall and the divertor material (Yang et al. 2017; Andruczyk et al. 2020). Liquid metal such as lithium creates a shielding layer when being in contact with plasma, reducing the thermal load on the structure (Andruczyk et al. 2020). A PFC in form of a capillary-porous tungsten mesh filled with lithium is able to withstand higher heat loads than similar existing solid materials, which has been shown in a number of studies (Evtikhin et al. 2002b; Zuo et al. 2011).

Capillary-porous system (CPS) is a common way to create a renewable liquid metal layer. CPS are made from a tungsten wire with a thickness of 10–100 µm with a cell size of 15 and 100 µm (Evtikhin et al. 2002a). When the CPS is immersed in lithium, capillary force draws in the liquid metal, filling the space between the wires. However, the CPS themselves need a base structure to which they will be attached (Lyublinski et al. 2016). This base structure should demonstrate high thermal conductivity, good machinability, corrosion resistance in Li and acceptable cost.

The simplest option is to integrate a CPS and a solid substrate into one tungsten wire-based material, in which one part is a CPS filled with a liquid metal and another is a solid material strengthened with tungsten wires (Popov et al. 2024). A composite material based on a tungsten wire should have a metal matrix that can be easily joined to steel by welding or brazing. A tungsten composite material with a steel matrix (WSS) will have an increased thermal conductivity compared to pure steel. Steel matrix will allow to decrease the cost of the material and ease its processability. Such material can also be welded to other structural elements.

Composites based on a tungsten wire have been already applied in engineering. In the case of thermonuclear energy, two types of materials have recently been developed: W/W(f) and W/Cu (De Luca et al. 2023; Riesch et al. 2024). The first type is tungsten reinforced with tungsten fiber (Du n.d.). To manufacture tungsten-based materials the CVD method is used. In case of the W/W(f) material, after tungsten hexafluoride gas is passed through a wire yarn specimen, a layer of deposited tungsten starts growing, filling the gaps between the wires (Dushik et al. 2018; Lau et al. 2024; Piskarev et al. 2024). The W/Cu material is obtained by infiltration from a copper melt, hot isostatic pressing and other methods (Saito et al. 2002; De Luca et al. 2023). As a result, pure copper solidifies in a porous tungsten structure. Two elements in the W-Cu system are insoluble in each other thus no interaction occurs during these processes.

Tungsten wires are used for strengthening of nickel alloys. The WNi composites demonstrates high mechanical properties (Warren et al. 1979). However cracks propagate in the interaction layer due to the limited solubility, the existence of intermetallic compounds (IMC) in the W-Ni binary system and a difference in CTE (Roy and Pastein 1974; Arai et al. 1989). After the exposure to high temperatures IMC layer significantly grows, causing the breakdown of a matrix–wire bond.

The use of steel as a matrix is difficult due to the interaction of tungsten with iron, chromium and nickel with the formation of IMC. In (Kumar 2013) the interaction between the W wire and the steel matrix in the WSS composite obtained by casting technique is described. Additionally, the diffusion coefficients and growth rates of the $(Fe,Cr)_7W_6$ IMC layer during annealing were presented. The most interesting result is that casting of $FeNi_2$ alloy suppresses the IMC layer formation on the W wire surface. However all commonly used steels were prone to form IMC and carbides around the W wire.

Various technologies such as plasma-spraying, laser cladding, spark plasma sintering, hot pressing and additive technologies were proposed to develop WSS composite and functional graded materials (Weber et al. 2013; Matějíček et al. 2015; Chen et al. 2018, 2021; Koller et al. 2018; Tan et al. 2019; Ganesh et al. 2023). Plasma-spraying and laser cladding methods are able to overcome the IMC formation, however they suffers from technological difficulties and have high production cost. These results evidence that it is possible to control the manufacturing parameters (time, temperature, pressure etc.) to obtain the optimal structure.

The matrix material for WSS composite is a crucial part of the design. AISI 316LN steel is the base material for the ITER construction. On the other hand ferritic-martensitic steels are more preferable due to higher radiation resistance. The reduced activation ferritic-matrensitic (RAFM) steel will eventually replace austenitic steel to guarantee radiation safety. Hence, two types materials for the matrix – austenitic 316LN and conventional 420 steels were chosen for this investigation.

As shown in (Kumar 2013), casting of the overheated steel melt at 1550 °C results in active interaction and a partial dissolution of the W wire. To reduce the interaction time, it is possible to use the infiltration method followed by fast cooling. The steel melt can be drawn in by the capillary forces in the CPS the same way as the liquid lithium is drawn.

The aim of this work is to propose the scalable technology for the WSS composite production. In this paper, the melt infiltration method is used to manufacture a composite based on tungsten mesh with a matrix of two types of steel. Since this method depends on the wetting angle between the two materials (Kainer 2006; Contreras Cuevas et al. 2018), this study also investigates the wetting of a tungsten substrate by steel melt, and the obtained structure.

Materials and methods

Wetting of tungsten by molten steel

The experimental setup of the modified dispensed drop method is shown in Fig. 1. Two types of stainless steel (SS) AISI 420, AISI 316LN and pure W were used as initial materials. Their chemical compositions are shown in Table 1.

Table 1. Materials chemical composition

Material	Content, wt.%							
	Fe	Cr	C	Ni	Ti	Mo	W	Other
AISI 420	Bal.	12–14	0.16–0.25	<0.6	-	-	-	<0.6Mn
AISI 316LN	Bal.	16–18	0.02	10–14	0.05	2–3	-	0.1–0.3N
W	-	-	-	-	-	-	>99.99	0.01(Fe+P+O_2)

Steel pieces with a weight of 0.6–0.7 grams were placed in a quartz crucible with an inner diameter of 4 mm and a nozzle diameter of 1.6–1.8 mm. Temperature was measured by a thermocouple places near the crucible nozzle. Austenitic 316LN steel was heated up to the temperature of 1450–1470 °C, SS420 was heated up to 1550–1560 °C. The steel was being melted for 2 minutes to ensure that the liquid is homogenous. Then, high-purity argon was introduced into the quartz crucible. The melt was squeezed out on a cold tungsten 20×20×1 mm^3 plate. In the experiment, W substrate inevitably heats up to the temperature of 500–650 °C due to the radiation from the injector Mo heaters above it. The temperature gradient on the surface measured using thermocouples placed in the center and at the edge of the sample was no more than 30 °C.

The contact wetting angle was calculated in the ImageJ program. To obtain valid results, wetting angle was calculated on 5 experiments for the each of the steel types. The tungsten was grounded on a diamond disc with a grain size of 1800 before the experiment.

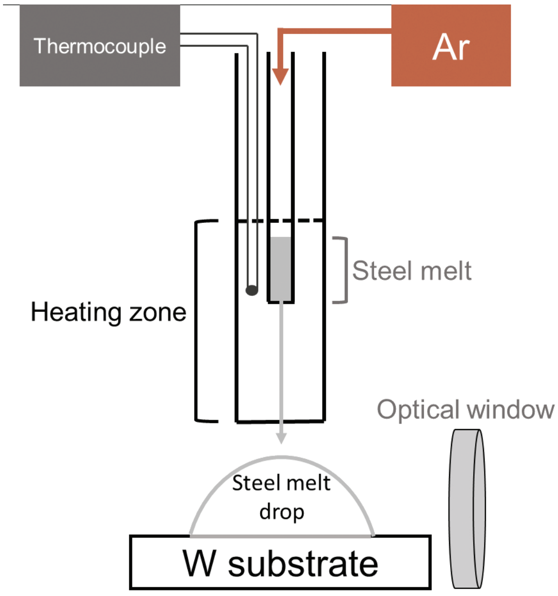

Figure 1. Experimental setup to measure wetting angle.

Interaction features study

The interaction study is divided into two parts: non-isothermal and isothermal. The time-temperature modes are shown in Table 2. In all experiments melt volume was equal to the one of the substrate (50 mm^3). In the non-isothermal experiment, only SS420 steel was injected onto W, whereas in isothermal experiments, both 420 and 316LN steels were melted directly onto W.

Table 2. Time-temperature modes for the specimens

Experiment type	W temperature, °C	Melt temperature, °C	Treatment
Non-isothermal (Injection)	650	1550	No exposure
Isothermal (Furnace)	1500	1500	No exposure
			No exposure
	1550	1550	10 min exposure
			10 min exposure

Infiltration of tungsten mesh by steel

The infiltration of the tungsten mesh by molten steel was carried out in an arc furnace. The experimental scheme is shown in Fig. 2. The furnace chamber was cleaned three times by evacuating air and replacing it with high purity argon. After filling the chamber with argon, zirconium getter was melted to remove residual oxygen. The steel was arc melted on a water-cooled copper crucible until a homogeneous melt was obtained.

Five layers of the tungsten mesh with a cell size of 1 mm manufactured by OFOLAN Metal Wire Mesh Manufacturing from a wire with a diameter of 100 microns were fixed between two tungsten plates. The specimen size was approximately 40×20×2 mm^3. The mesh was placed next to the steel. After the melting of the steel, the arc was moved to the edge of the melt. Thus, melt pool was pushed towards the mesh specimen. The melt that was in contact with the sample spontaneously infiltrated the mesh. To keep the interaction period as short as possible, the arc melting was stopped immediately after the contact.

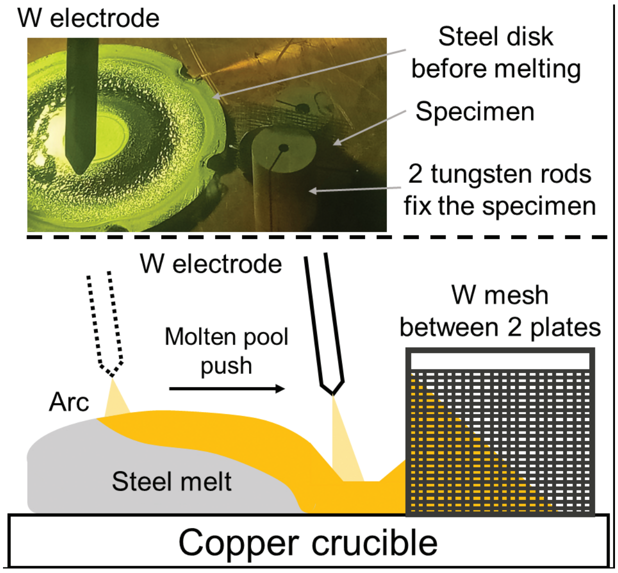

Figure 2. Schematic representation of the infiltration experiment.

Microstructure and phase analysis

For the microstructure investigation, the specimens were cut in half by a Struers Minitom low-speed cutting machine. Afterwards the specimens were prepared for microstructure and phase analysis according to the standard procedure: grinding and polishing on diamond paste with a size of 3–1 µm. The microstructure was studied using scanning electron microscopy (SEM) via JEOL JSM–6610LV and Carl Zeiss EVO 50 with energy dispersive spectrometry (EDS) on the Oxford Instruments INCA x-act instrument. The phase composition of the remaining samples was analyzed using X-ray phase analysis on the Brucker D8 Discover device.

Results and discussion

Wetting of cold W substrate by 420 and 316LN melt

The melt temperature range was selected based on the result of a series of experiments that involved heating a 316LN steel melt with a liquidus temperature of 1400 °C. It was found that heating higher than 1470 °C does not have a noticeable effect on the wetting angle, while actually causing the droplet spraying. When heated below 1440 °C, the droplet starts to crystallize before coming into contact with tungsten. Similarly, for steel 420 with a liquidus of about 1500 °C, the injection temperature of 1550 °C was selected.

The standard sessile drop method used in number of works (Pitak and P’yanykh 1965; Xuan et al. 2015) implies simultaneous heating of a substrate and liquid to the same temperature. In the previous work (Popov et al. 2024) we investigated the interaction of iron and steels with a tungsten substrate at temperatures close to the melting point. Under these conditions, the interaction leads to the complete wetting and the formation of a large number of intermetallic phases which are undesirable in terms of mechanical properties. Additionally the IMC formation could have affected the wetting by both increasing and decreasing it (Protsenko et al. 2001).

In this work, the modified dispensed drop method was used to simulate the wetting process when the melt is heated to a temperature higher than the substrate. Heating zones are isolated from each other which allows to control the temperatures of the melt and the substrate separately. However, the injector heating zone is located close to the substrate which causes the heating of the substrate by radiation. The wetting process after the injection of the steel melt on tungsten substrate is shown in Fig. 3.

In (Long et al. 2024) the wetting was measured by a similar method, however the melt was heated by high-frequency induction melting. This type of heating suits well for their purpose due to their substrate is non-conductive. The method was reworked to investigate the wetting of metal substrate.

The wetting angle (θ) of tungsten for 316LN steel ranges from 55–77°, while steel 420 ranges from 75–94°. At the same time, the average temperature of tungsten in the first case was 520 °C, and 650 °C in the second. The major source of error is the dissymmetry of the droplet after the contact with tungsten. The crucible nozzles have slightly different shapes and diameters which affects the shape of the droplet. The average contact wetting angle value is 69° for SS316LN and 83.2° for SS420.

These results could be compared with those of (Long et al. 2024), where steel melt wets the alumina substrate. Both in our investigation and in mentioned work, the contact angle has a dynamic stage and static stage. However, in this study the melt rapidly reacts with the substrate, after which solidification follows. The contact angle was measured right after the melt form a drop shape on substrate (~0.5 sec after injection).

The maximum melt rise in a capillary (h) is calculated using the Jurin formula (1). This allows to estimate the tungsten mesh dimensions for the next infiltration experiment.

$$h = \frac{2\gamma_{lv}\cos\theta}{\rho g r} \tag{1}$$

Here γ_{lv} – liquid-vapor surface energy, g – gravitational acceleration, ρ – density, r – capillary diameter. The data for surface energy was obtained from the articles (Choe et al. 2014; Klapczynski et al. 2022). Thus, the estimated h

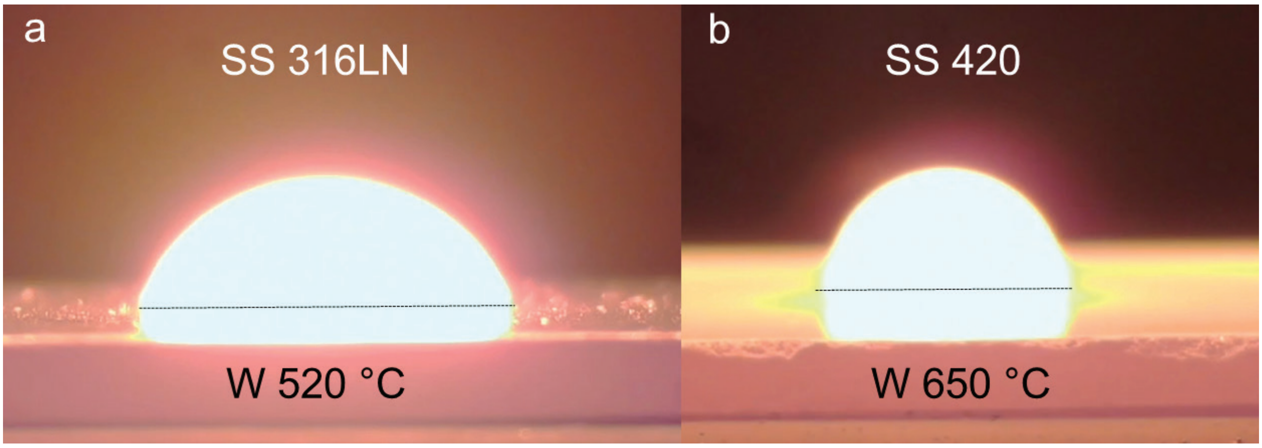

Figure 3. Tungsten substrate at 500–660 °C wetted by **a)** 316LN at 1460 °C, **b)** SS420 at 1520 °C.

value for the 1 mm capillary mesh is h = 23 mm for steel 316LN and h = 13 mm for steel 420.

The contact time of the liquid melt with tungsten was too short to form any detectable interaction layer. Due to the small volume of steel and the high thermal conductivity of relatively cold tungsten a complete crystallization of the droplet was observed within 1–2 seconds.

Interaction layer after injection of SS420 melt on cold tungsten

To analyze the interaction layer, the amount of molten steel was increased so that the volume of steel and tungsten was the same. This increases the cooling time of the droplet after the injection so that the materials interact more actively with the dissolution of W in the melt. The SS420 steel droplet microstructure on the W substrate is shown in Fig. 4.

A reaction zone (location 1 in Fig. 4) was observed along the surface of tungsten in the form of a continuous layer of IMC with the composition of point 1 – 46Fe-40W-14Cr at.%. These IMC were also detected at a distance of about 100 µm from the surface of tungsten. The steel itself is enriched with tungsten. The chemical composition of the steel matrix in point 2 is 77Fe–9W-14Cr at.%. The phases with composition of point 1 are most likely the µ phases $(Fe,Cr)_7W_6$. In the Fe-Cr-W ternary system point 2 chemical composition corresponds to the mixture of an α solid solution and the λ $(Fe,Cr)_2W$ phase. Due to the small size of the crystals near point 2 it is impossible to define the phase composition using EDS and XRD data.

In addition to the cracks, a porous zone is observed in location 2 in Fig. 4. According to the EDS data, the chemical composition of phases in point 3 is 53Fe-28W-19Cr at.%. These small crystals have lower tungsten content in comparison with the point 1. Their chemical composition is much closer to the λ $(Fe,Cr)_2W$ phase. In the steel matrix in point 4 with composition of 80Fe-7W-13Cr at.% the tungsten content is lower than in point 3. It seems that this zone was isolated from tungsten by a pore, thus tungsten was forced to diffuse from a greater distance.

A well-distinguishable IMC reaction layer with a thickness of about 10 µm is formed on tungsten surface. A crack between tungsten and steel is clearly visible in the Fig. 4 in location 3. The difference in CTE between the two materials causes high thermal stresses at the boundary which in turn causes the crack propagation. The IMC and W are prone to cracks due to their brittleness.

The concentration of tungsten drops to zero at a distance of about 250 µm from the surface of the plate. Fig. 5 shows the EDS elemental distribution maps. They clearly indicate that the tungsten is present in both the IMC phases and steel. Iron does not diffuse into tungsten, while a small amount of chromium dissolves in tungsten.

The IMC layer grow during long-term contact of the melt with tungsten

To analyze the phase evolution during the interaction of molten steel and tungsten, two types of steels were melted on the surface of tungsten at 1500 and 1550 °C. In the last case, the specimen was held for 10 minutes at a target temperature. This experiment simulates the interaction of steel and tungsten heated up to the same temperature above the steel liquidus point after which fast cooling or long exposure follows.

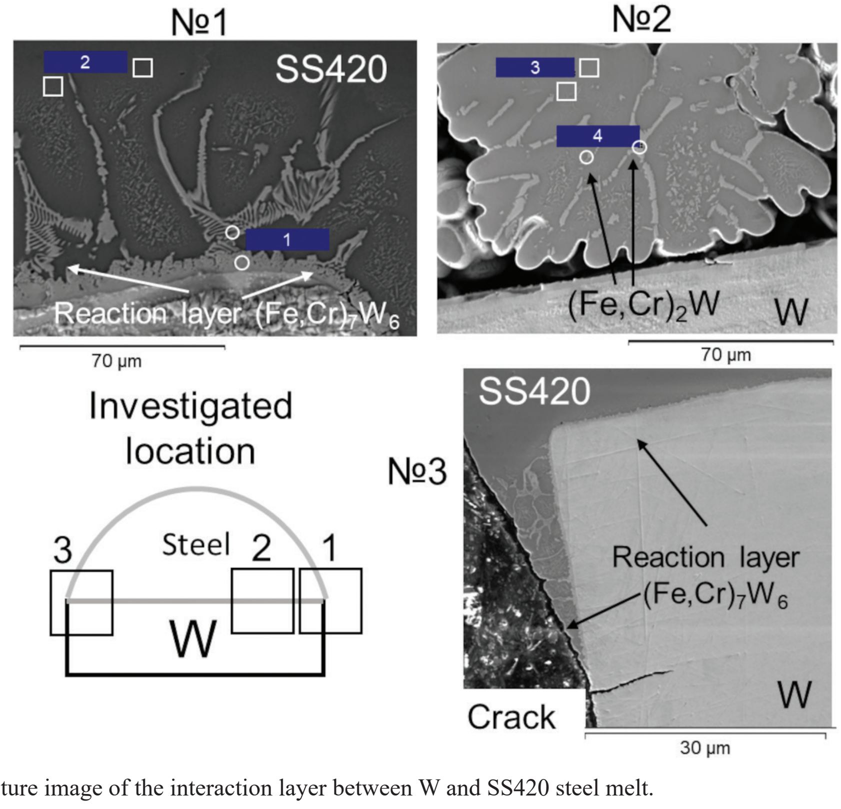

Figure 4. Microstructure image of the interaction layer between W and SS420 steel melt.

The microstructures of the specimens W420 and W316LN are shown in Fig. 6 together with the chemical composition of the IMC. Based on our previous results (Popov et al. 2024) and literature data (Kumar 2013) these are μ Fe_7W_6 phases.

Considering the SS420 interaction with W, the IMC layer increases slightly in size with increasing temperature and time. The chromium content reduces due to the diffusion into tungsten.

The temperature of 1500 °C for steel SS420 is the liquidus point, while for SS316LN it exceeds liquidus by 100 degrees. Thus, the interaction of austenitic steel at the same temperature is much more intense. The thickness of the IMC layer at the boundary of tungsten and steel 420 and 316LN is about 5 and 10 microns respectively. Due to the overheating, high diffusion and dissolution rate of tungsten in the SS316LN melt the erosion occurs in W316LN specimen's case.

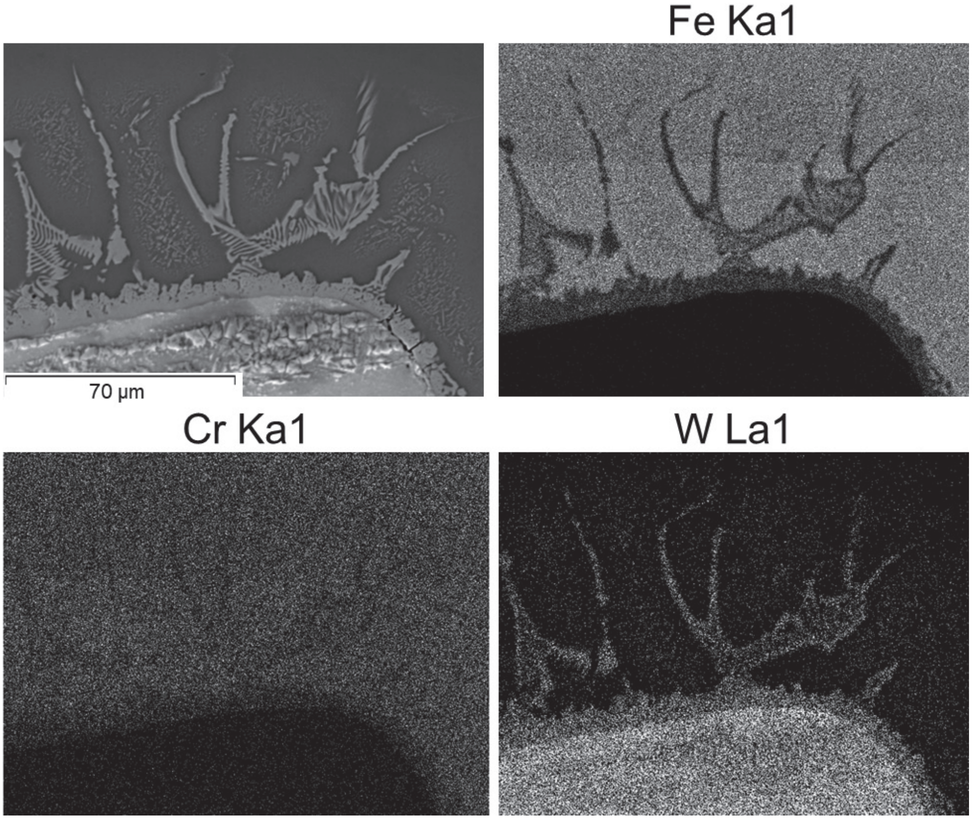

Figure 5. EDS elemental distribution maps of W420 specimen.

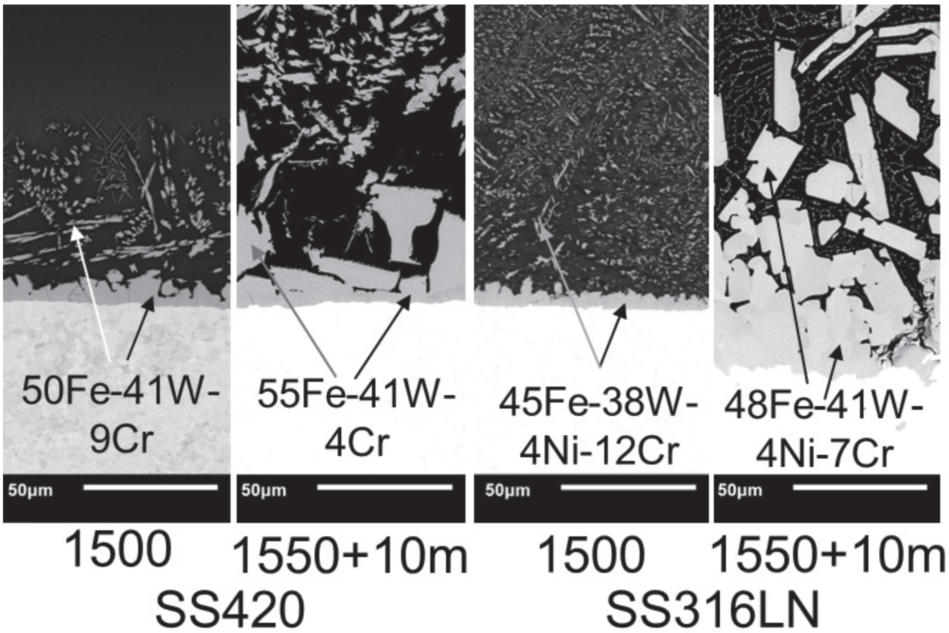

Figure 6. Microstructure of SS420 and SS316LN melted on W at 1500 followed by cooling and at 1550 °C with 10 minutes exposure.

Phase composition was analyzed on the specimens where tungsten was removed by cutting and grinding so that only steel and interaction zone remained. Peaks from the two phases – BCC iron and μ phase – were observed in the XRD spectra. The presence of the λ phase is hard to detect due to its small size. Every mentioned specimen was analyzed via XRD with a spanning speed of 0.05 °/sec to properly identify the small-sized IMC. In Fig. 7 the XRD spectra for specimen W420 obtained via melting at 1500 °C presented. It is evident that due to small size of IMC the peaks are under background especially when scanning speed is relatively high. The pure tungsten does not have peaks at 30–44°, while Fe7W6 with trigonal $\overline{R}3m$ space group have numerous peaks with high intensivity.

A significant IMC layer thickness increase was observed when the melt was overheated above the liquidus by 150 °C. Thus, in order to reduce the interaction layer, it is necessary to prevent overheating of the melt and reduce the interaction time of the melt with tungsten. The IMC formation could be suppressed by rapid cooling (quenching). However, in a similar work (Kumar 2013) the annealing for 100 hours at 1000 °C caused the decomposition of a metastable solid solution.

Infiltration of tungsten mesh

Capillary force draw steel melt into the mesh. The melt crystallizes after a short period of time. The experiments distinguish characteristic is that the tungsten mesh was set vertically to demonstrate the structural differences across different zones. The lower part of the mesh was in contact with a water-cooled copper substrate, while the middle part was in contact with the most of the heated melt. The photo of the specimen after infiltration is shown in Fig. 8. The upper part of the mesh was not filled with steel. At the cross-section the wetting effect between steel and tungsten could be observed. The melt rose along the plate wall sustaining a smooth contact with it.

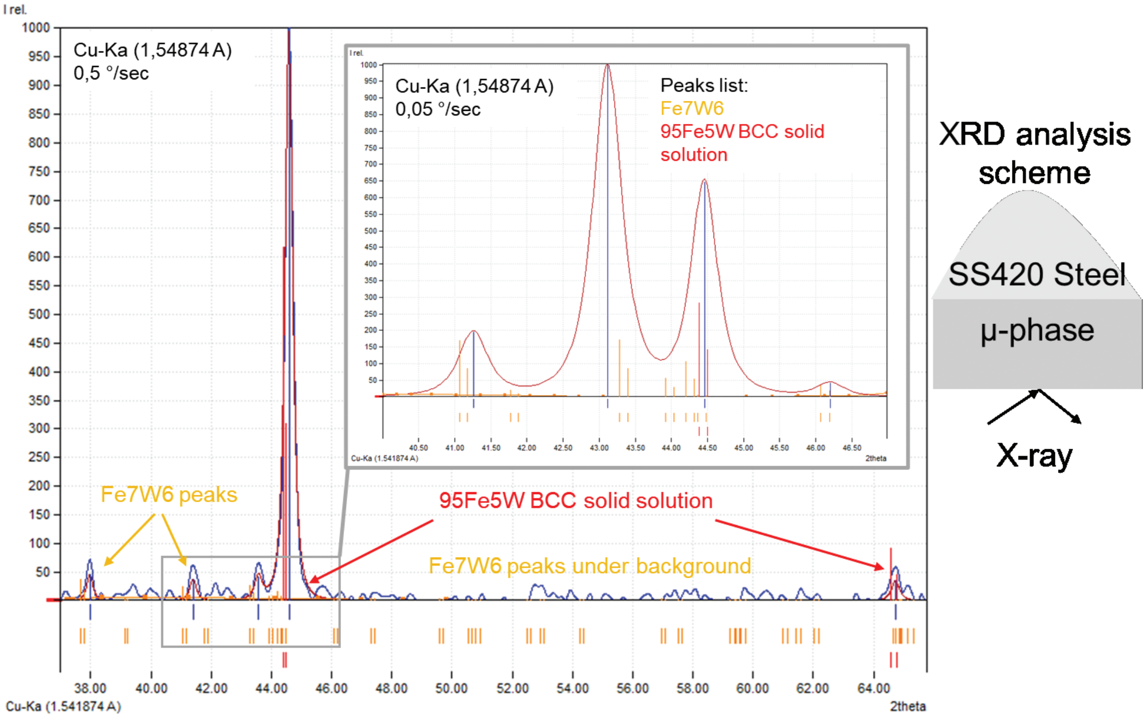

Figure 7. XRD pattern of W420 – 1500 °C without exposure. The Figure represents the results of the analysis at two scanning speeds – 0.5 and additional 0.05 °/sec scanning at the 2θ angles 30–50°.

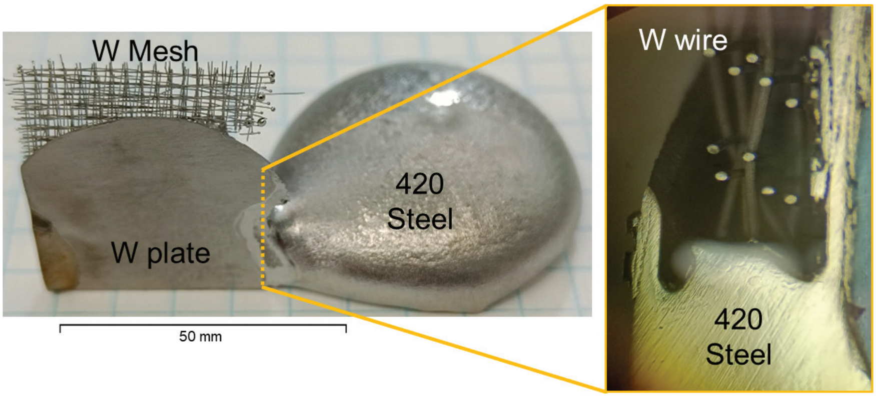

Figure 8. Specimen of tungsten mesh infiltrated with SS420 in arc melting furnace.

Fig. 9 shows a schematic representation of three thermal zones. The cross-section of the specimen can be divided into the three main zones: cold, hot and quenching zone. A feature of arc melting is the high temperature gradient of the melt. The lower part of the steel ingot that was in contact with a cold substrate during melting remained solid. At the same time the outer edges of steel heated directly by the arc were liquid.

The flow is driven by the capillary force which is proportional to the wetting angle. The liquid infiltrates the mesh precisely from the upper part of the melt where it has lower viscosity. Thus, the area of contact of the melt with tungsten is labeled hot zone.

The part of the melt that is in contact with copper has a temperature near the melting point of steel. The crystallization front moves from this zone. In this area the cooling rate is also higher than in the other zones which causes quenching. Thus, this zone named as quenching zone.

The cold zone is referring to the upper area of specimen which is not in the direct contact with a melt drawn from the top of the steel ingot. It has a lower temperature than the hot zone. Since tungsten has high thermal conductivity, a part of the melt begins to crystallize around the tungsten wire and plates. At a distance from the hot zone, the gap between the wire and the plates is completely filled with crystallized steel. This zone has the lowest cooling rate among others.

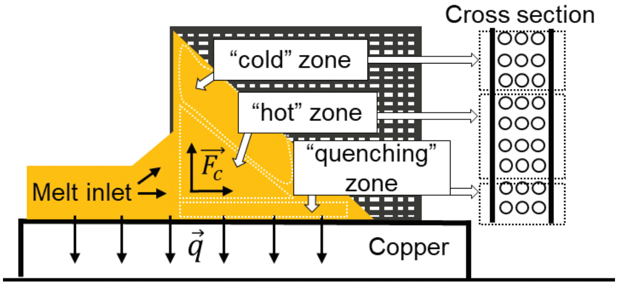

Figure 9. Schematic representation of infiltration process.

The microstructure of the three zones is shown in Figs 10–13. Despite the high temperature in the hot zone, the thickness of the intermetallic layer around the tungsten wire in the hot and cold zones is in the range of 5–8 μm. In the quenching zone, the thickness is lower – about 2–3 μm. Voids from missing tungsten wire were found in the structure of the composite. It is most likely that they were pulled out during grinding.

Chemical analysis of the interaction zone of all zones revealed that intermetallic compound has a chemical composition similar to the previously observed $(Fe,Cr)_7W_6$. Particles with high tungsten content precipitate around the intermetallic layer. The size of these particles is less than 1 μm, which makes it impossible to determine their exact chemical composition by the EDS method. A similar microstructure is observed on the mesh infiltrated with 316L steel in Fig. 11. The chemical composition of the interaction zone of W316L specimen is 38W-45Fe-4Ni-13Cr at.% which is similar to the composition obtained earlier when 316LN steel sample melted on tungsten at 1500 °C.

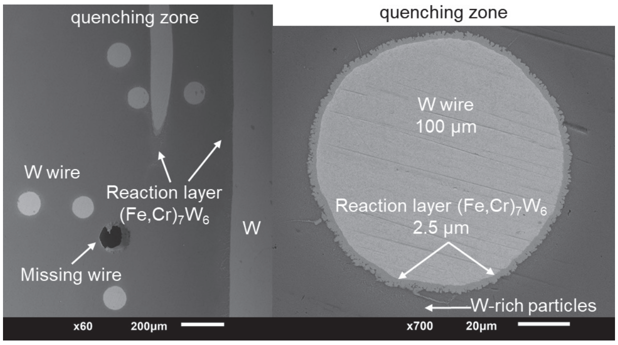

Figure 10. Cross-section of quenching zone of W420 composite.

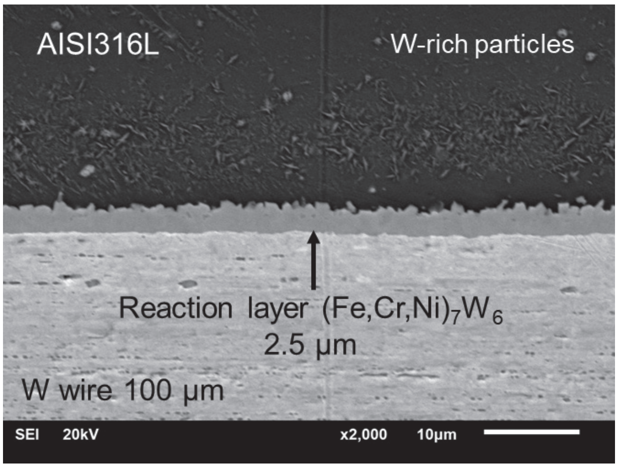

Figure 11. Longitudinal cross-section of quenching zone of W316L composite.

In the hot zone, tungsten is intensively dissolved in the melt. The typical structure in the hot zone shown in Fig. 12. The wire diameter is reduced from 100 μm to 40 μm. The IMC layer around the wire increases slightly by 1–3 μm compared to the quenching zone. A distinctive feature of the zone is the presence of a large number of tungsten-based IMC in the steel volume. In this area, the melt is highly enriched with tungsten due to its active dissolution. Additionally, lower cooling rate does not suppress diffusion processes, causing IMC precipitate from the melt.

The cold zone is characterized by the minimal interaction of tungsten with the melt. The microstructure of the W420 specimen shown in Fig. 13 demonstrates a 5–8 μm thick IMC zone. A few intermetallic phases were identified near the wire. Unlike the hot zone case, these phases are formed only in a small area around the wire due to the lower temperature.

Wire thickness distribution in form of a graph of diameter (d) vs. specimen height (H) is shown in Fig. 14. Wire thickness sharply decreases from the bottom of the W420 specimen to its centre. The thickness then slowly reaches its initial value near the top of the specimen. The quenching zone is relatively narrow compared to the hot and cold zones. At a height of 3–4 mm the erosion is the most intense.

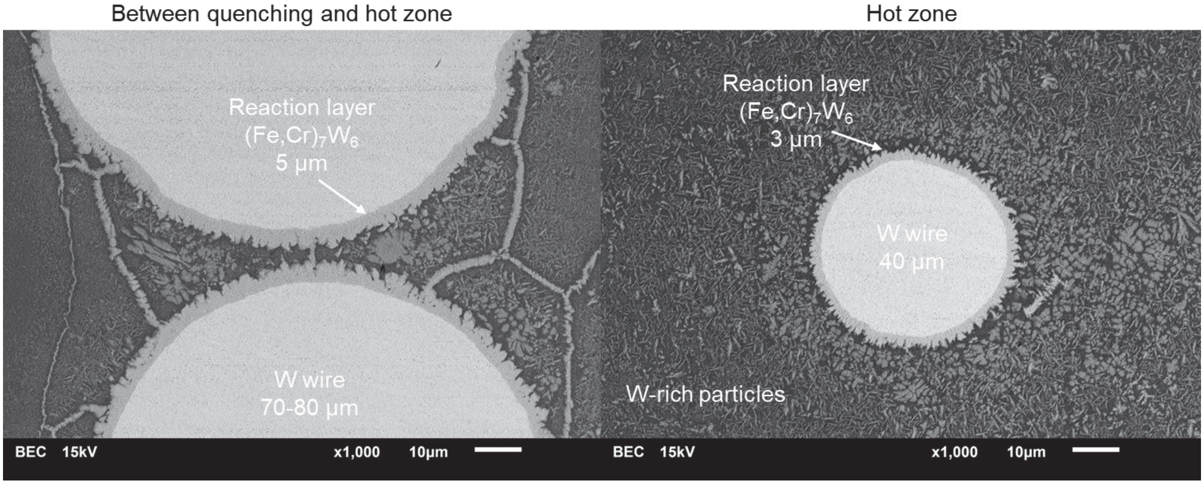

Figure 12. Cross-section of hot zone of W420 composite.

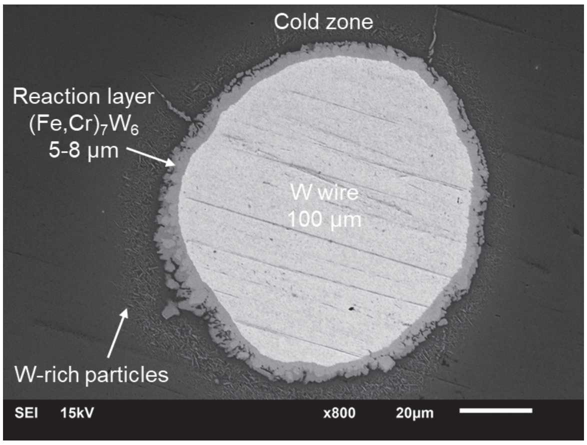

Figure 13. Cross-section of cold zone of W420 composite.

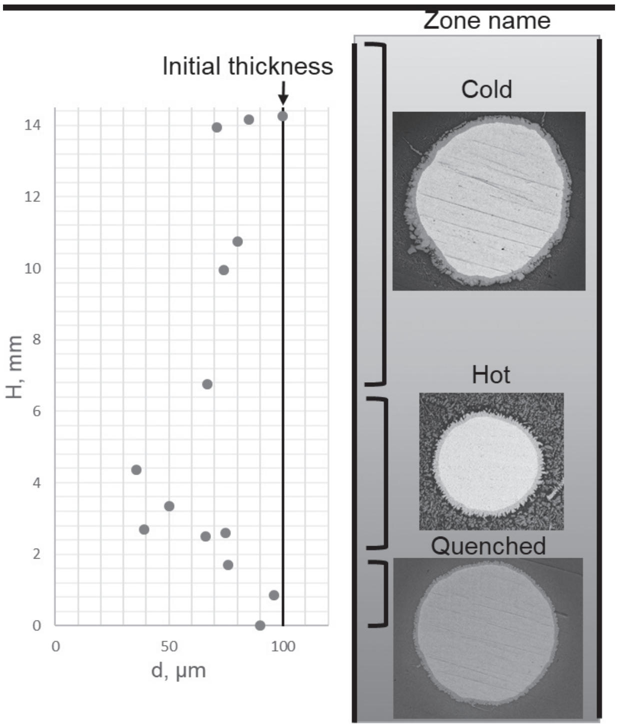

Figure 14. Wire thickness at different zones of W420 specimen and examples of zone microstructure.

Comparison of experimental results

A comparison of the structures of the three zones with different thermal effects indicates that the amount of dissolved tungsten is the most significant difference. The diameter of the wire remained unchanged, and the thickness of the interaction layer turned out to be the thinnest in the cold and quenching zones. Thus, if infiltration occurs at a temperature close to the melting point of steel, the formation of the undesirable IMC phases will be minimal.

This is also supported by the minimal interaction and dissolution observed in the microstructure of steel melted on tungsten at 1500 °C. Melting steel on tungsten in a vacuum furnace result in a lower cooling rate and a longer interaction time than infiltration. For example, 316LN steel was in a liquid state for less than 1.5 minutes when it was being melted on tungsten at 1500 °C. Nevertheless, the interaction layer did not exceed 10 µm. The time of infiltration process is about a few seconds, after which it takes from 20 to 30 seconds to cool down to the last visible radiation temperature of 600 °C.

High melt temperatures cause severe dissolution of tungsten. The melt with high tungsten content crystallizes in form of the Fe_7W_6 type IMC layer on the tungsten surface. During cooling some of the IMC precipitates form a solid solution. The second λ type IMC do not play a significant role in the structure of the material. This may be the result of a low diffusion rate in a solid state and a diffusion barrier in form of a IMC layer on tungsten. Chemical and phase analysis show that the interaction layer consists only of an intermetallic compound of the µ type, which corresponds to the results of the article (Kumar 2013).

In another work (Warren et al. 1979) the connection between tungsten wire and steel was obtained by hot isostatic pressing (HIP) at a lower temperature of 1200 °C. However, even in the case of HIP, diffusion processes cause the formation of a Fe_7W_6 layer with a thickness of 10 µm.

It can be concluded that the structure with minimal interaction formed in quenching zone. Thus the melt infiltration require the conditions similar to bulk amorphous materials (BMG). The BMG were successfully manufactured by suction casting (Dandliker et al. 1998; Wall et al. 2006; Ryu et al. 2022) with a cooling rate up to 10^4 K/s (Pawlik et al. 2008; Kozieł et al. 2020). This technology as well as drop casting could be used to improve the infiltration method.

Conclusion

A new approach to the manufacturing of a composite based on a tungsten mesh and a steel matrix presented in the work. The infiltration of the tungsten mesh by molten steel was tested on the tungsten mesh with a cell size of 1 mm and a 100 µm wire diameter. Two types of stainless steels 316LN and SS420 are proposed as a composite matrix.

The average wetting angle between cold tungsten and SS316LN is 69°, and 83.2° for SS420. Calculated maximal height of the melt rise is 23 mm for 316LN and 13 mm for steel 420.

Short-term and long-term interaction of tungsten with a melt of both steel types cause the formation of $(Fe,Cr)_7W_6$ layer. The thickness of the layer during short-term interaction is about 5 µm for W420 and 10 µm for W316LN specimens. Rate of tungsten dissolution is strongly affected by the melt overheating above liquidus point and exposure time. The overheating above liquidus by 150 °C cause the rapid dissolution of tungsten followed by formation of thick brittle IMC layer. This evidence that shot-term interaction and fast cooling could prevent the IMC layer grow.

The tungsten mesh with a cell size of 1 mm was infiltrated with the 420 and 316LN steel melt. Specimens with dimensions of 40×20×2 mm were obtained by infiltration in arc melting furnace in Ar atmosphere. The structure can be divided into three main zones by their cooling rates and the average melt temperature. The thickness of the layer in the cold and hot zones differs from 2.5 to 8 µm. The overheated melt in the hot zone dissolves tungsten, causing the decrease of the wire diameter from 100 µm to 40 µm. In zones, where the melt was at lower temperature, the interaction did not significantly reduce the wire diameter.

Funding

This work has been supported by the grants the Russian Science Foundation, RSF 24-23-00111 https://rscf.ru/project/24-23-00111/.

References

- Andruczyk D, Maingi R, Hu JS, Zuo GZ, Rizkallah R, Parsons M, Shone A, O'Dea D, Kapat A, Szott M, Stemmley S, Sun Z, Xu W, Meng XC, Lunsford R, Gilson EP, Diallo A, Tritz K, The EAST team (2020) Overview of lithium injection and flowing liquid lithium results from the US–China collaboration on EAST. Physica Scripta T171: 014067. https://doi.org/10.1088/1402-4896/ab6ce1
- Arai T, Kobayashi T, Itagaki M, Takatsu S, Shibuki K, Tsukamoto T (1989) Multi-layer Coatings for Preventing Diffusion of Nickel into Tungsten Fiber. Tetsu-to-Hagane 75: 1493–1500. https://doi.org/10.2355/tetsutohagane1955.75.9_1493
- Chen H, Ye L, Han Y, Chen C, Fan J (2021) Additive manufacturing of W–Fe composites using laser metal deposition: Microstructure, phase transformation, and mechanical properties. Materials Science and Engineering A 811: 141036. https://doi.org/10.1016/j.msea.2021.141036
- Chen Z, Sawa Y, Hashimoto N (2018) Development of F82H composite materials with a high thermal conductivity. Nuclear Materials and Energy 16: 133–136. https://doi.org/10.1016/j.nme.2018.06.017
- Choe J, Kim HG, Jeon Y, Park HJ, Kang Y, Ozawa S, Lee J (2014) Surface Tension Measurements of 430 Stainless Steel. ISIJ International 54: 2104–2108. https://doi.org/10.2355/isijinternational.54.2104
- Contreras Cuevas A, Becerril EB, Martínez MS, Ruiz JL (2018) Metal Matrix Composites: Wetting and Infiltration. Springer International Publishing, Cham. https://doi.org/10.1007/978-3-319-91854-9
- Dandliker RB, Conner RD, Johnson WL (1998) Melt infiltration casting of bulk metallic-glass matrix composites. Journal of Materials Research 13: 2896–2901. https://doi.org/10.1557/JMR.1998.0396
- De Luca, Fanelli P, Paoletti D, Stefanini C, von Müller A, Feichtmayer A, Vivio F, Belardi V, Dose G, De Sano G, Roccella S, Calabro G, You J-H, Neu R (2023) Pre-conceptual design of a PFC equipped with a W lattice armour for first wall limiters in the EU-DEMO fusion reactor. Fusion Engineering and Design 191: 113742. https://doi.org/10.1016/j.fusengdes.2023.113742
- Du J (n.d.) A Feasibility Study of Tungsten-Fiber-Reinforced Tungsten Composites with Engineered Interfaces. PhD thesis, Max-Planck-Institut für Plasmaphysik, Munchen, Germany, 132 pp.
- Dushik VV, Rozhanskii NV, Lifshits VO, Rybkina TV, Kuzmin VP (2018) The formation of tungsten and tungsten carbides by CVD synthesis and the proposed mechanism of chemical transformations and crystallization processes. Materials Letters 228: 164–167. https://doi.org/10.1016/j.matlet.2018.06.003
- Evtikhin VA, Vertkov AV, Lyublinski IE, Khripunov BI, Petrov VB, Mirnov SV (2002a) Research of lithium capillary-pore systems for fusion reactor plasma facing components. Journal of Nuclear Materials 307–311: 1664–1669. https://doi.org/10.1016/S0022-3115(02)01132-7
- Evtikhin VA, Lyublinski IE, Vertkov AV, Mirnov SV, Lazarev VB, Petrova NP, Sotnikov SM, Chernobai AP, Khripunov BI, Petrov VB, Prokhorov DYu, Korzhavin VM (2002b) Lithium divertor concept and results of supporting experiments. Plasma Physics and Controlled Fusion 44: 955–977. https://doi.org/10.1088/0741-3335/44/6/322
- Gago M, Kreter A, Unterberg B, Wirtz M (2020) Synergistic effects of particle and transient heat loads on ITER-grade tungsten. Physica Scripta 2020: 014007. https://doi.org/10.1088/1402-4896/ab3bd9
- Ganesh V, Dorow-Gerspach D, Bram M, Coenen JW, Wirtz M, Pintsuk G, Theisen W, Linsmeier C (2023) Processing and Properties of Sintered W/Steel Composites for the First Wall of Future Fusion Reactor. Journal of Nuclear Engineering 4: 177–192. https://doi.org/10.3390/jne4010014

- Guseva MI, Suvorov AL, Korshunov SN, Lazarev NE (1999) Sputtering of beryllium, tungsten, tungsten oxide and mixed W–C layers by deuterium ions in the near-threshold energy range. Journal of Nuclear Materials 266–269: 222–227. https://doi.org/10.1016/S0022-3115(98)00819-8
- Kainer KU [Ed.] (2006) Metal Matrix Composites: Custom-made Materials for Automotive and Aerospace Engineering. 1st ed. Wiley. https://doi.org/10.1002/3527608117
- Klapczynski V, Le Maux D, Courtois M, Bertrand E, Paillard P (2022) Surface tension measurements of liquid pure iron and 304L stainless steel under different gas mixtures. Journal of Molecular Liquids 350: 118558. https://doi.org/10.1016/j.molliq.2022.118558
- Koller M, Kruisová A, Mušálek R, Matějíček J, Seiner H, Landa M (2018) On the relation between microstructure and elastic constants of tungsten/steel composites fabricated by spark plasma sintering. Fusion Engineering and Design 133: 51–58. https://doi.org/10.1016/j.fusengdes.2018.05.056
- Kozieł T, Pajor K, Gondek Ł (2020) Cooling rate evaluation during solidification in the suction casting process. Journal of Materials Research and Technology 9: 13502–13508. https://doi.org/10.1016/j.jmrt.2020.09.082
- Kumar P (2013) Studies of Wire-Matrix Interaction in Some Tungsten Wire Reinforced Stainless Steels. University of Canterbury.
- Lau A, Mao Y, Shu R, Coenen JW, Poll M, Linsmeier C, Gonzalez-Julian J (2024) Combining chemical vapor deposition and spark plasma sintering for the production of tungsten fiber-reinforced tungsten (Hybrid – W_f/W). Advanced Engineering Materials: 2301929. https://doi.org/10.1002/adem.202301929
- Long Q, Wang W, Gao X (2024) Measuring dynamic nonreactive wetting behavior between interstitial-free molten steel and alumina. Metallurgical and Materials Transactions B 55: 1762–1772. https://doi.org/10.1007/s11663-024-03065-7
- Lyublinski IE, Vertkov AV, Zharkov MYu, Sevryukov ON, Dzhumaev PS, Shumskiy VA, Ivannikov AA (2016) Selection of materials for tokamak plasma facing elements based on a liquid tin capillary pore system. Journal of Physics: Conference Series 748: 012014. https://doi.org/10.1088/1742-6596/748/1/012014
- Matějíček J, Nevrlá B, Vilémová M, Boldyryeva H (2015) Overview of processing technologies for tungsten-steel composites and FGMs for fusion applications. Nukleonika 60: 267–273. https://doi.org/10.1515/nuka-2015-0049
- Pawlik P, Pawlik K, Przyby A (2008) Investigation of the cooling rate in the suction casting process. Reviews on Advanced Materials Science 18: 81–84.
- Pitak NV, P’yanykh NL (1965) Wetting of refractories by molten steel and slag. Refractories 6: 243–248. https://doi.org/10.1007/BF01290824
- Popov N, Suchkov A, Zharkov M, Kirillova V, Bazhenov A, Fedotov I, Bajenova I, Khvan A, Kozlov I, Vertkov A, Sevryukov O (2024) Interaction of iron melt with tungsten and WFe composite structure evolution. Nuclear Energy and Technology 10: 189–198. https://doi.org/10.3897/nucet.10.129596
- Protsenko P, Terlain A, Traskine V, Eustathopoulos N (2001) The role of intermetallics in wetting in metallic systems. Scripta Materialia 45: 1439–1445. https://doi.org/10.1016/S1359-6462(01)01181-2
- Piskarev PYu, Rulev EV, Mazul IV, Krasilnikov A, Pisarev AA, Kuteev BV, Kolesnik MS, Dushik VV, Bobrov SV, Montak NV, Rubikov AA, Bukatin TN (2024) Coatings on a first wall plasma-facing surface: analysis and high heat flux testing on the «TSEFEY-M» e-beam facility. Problems of Atomic Science and Technology Ser Thermonuclear Fusion 47: 111–121. https://doi.org/10.1134/S1063778824130076
- Riesch J, von Müller A, Mao Y, Coenen JW, Böswirth B, Elgeti S, Fuhr M, Greuner H, Höschen T, Hunger K, Junghanns P, Lau A, Roccella S, Vanlitsenburgh L, You J-H, Linsmeier Ch, Neu R (2024) Progress in the development of industrial scale tungsten fibre-reinforced composite materials. Nuclear Materials and Energy 38: 101591. https://doi.org/10.1016/j.nme.2024.101591
- Roy C, Pastein S (1974) Development of oxide diffusion-barrier on refractory metals. Journal of Materials Science 9: 1004–1010. https://doi.org/10.1007/BF00570396
- Ryu WH, Kim KJ, Yoo GH, Park ES (2022) Alloy design strategy to improve fluidity of Zr-based bulk metallic glass for near-net-shape manufacturing. Journal of Alloys and Compounds 896: 162680. https://doi.org/10.1016/j.jallcom.2021.162680
- Saito S, Fukaya K, Ishiyama S, Sato K (2002) Mechanical properties of HIP bonded W and Cu-alloys joint for plasma facing components. Journal of Nuclear Materials 307–311: 1542–1546. https://doi.org/10.1016/S0022-3115(02)01169-8
- Tan C, Zhou K, Kuang T (2019) Selective laser melting of tungsten-copper functionally graded material. Materials Letters 237: 328–331. https://doi.org/10.1016/j.matlet.2018.11.127
- Wall JJ, Fan C, Liaw PK, Liu CT, Choo H (2006) A combined drop/suction-casting machine for the manufacture of bulk-metallic-glass materials. Review of Scientific Instruments 77: 033902. https://doi.org/10.1063/1.2179415
- Warren R, Andersson CH, Larsson LO (1979) Fibre/matrix interactions in a tungsten alloy wire-reinforced stainless steel composite. Composites 10: 121–125. https://doi.org/10.1016/0010-4361(79)90013-2
- Weber T, Stüber M, Ulrich S, Vaßen R, Basuki WW, Lohmiller J, Sittel W, Aktaa J (2013) Functionally graded vacuum plasma sprayed and magnetron sputtered tungsten/EUROFER97 interlayers for joints in helium-cooled divertor components. Journal of Nuclear Materials 436: 29–39. https://doi.org/10.1016/j.jnucmat.2013.01.286
- Xuan C, Shibata H, Zhao Z, Jönsson PG, Nakajima K (2015) Wettability of TiN by Liquid Iron and Steel. ISIJ International 55: 1642–1651. https://doi.org/10.2355/isijinternational.ISIJINT-2014-819
- Yang Q, Chen Z, Du Q, Xu H, Zuo G, Ren J, Hu J, Song Y, Li J, Ding F, Zakharov L (2017) Development of the flowing liquid lithium limiter for EAST tokamak. Fusion Engineering and Design 124: 179–182. https://doi.org/10.1016/j.fusengdes.2017.04.063
- Zuo GZ, Hu JS, Li JG, Luo NC, Zakharov LE, Zhang L, Ti A (2011) First results of lithium experiments on EAST and HT-7. Journal of Nuclear Materials 415: S1062–S1066. https://doi.org/10.1016/j.jnucmat.2010.08.052